

Graphical Abstract

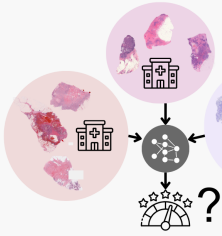
A protocol for evaluating robustness to H&E staining variation in computational pathology models

Lydia A. Schoenpflug, Nikki van den Berg, Sonali Andani, Nanda Horeweg, Jurriaan Barkey Wolf, Tjalling Bosse, Viktor H. Koelzer, Maxime W. Lafarge

A protocol for evaluating robustness to H&E staining variation in computational pathology models

Motivation

H&E staining varies within and across institutional datasets



→ How robust are trained CPath models to H&E staining variation?

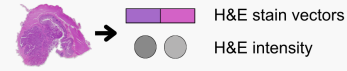
→ Does any staining condition consistently lead to better performance?

Evaluation Protocol

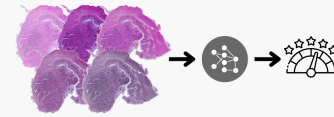
1 Select reference staining conditions



2 Characterize test set staining properties



3 Apply CPath model under simulated reference staining conditions



Exemplary Use Case

MSI classifiers (n=306 models) on SurGen hold-out test set (n=738 whole slide images):

- **Model performance:** AUC = 0.769-0.911
- **Robustness:** Min-max AUC range across conditions = 0.007-0.079
- **Correlation performance-robustness:** $r = -0.22$, 95% CI = [-0.31, -0.11]
- **Impact of staining condition on performance:**
 - No staining condition was best consistently
 - Trend toward higher performance in high intensity and low color similarity condition

Conclusions

Our evaluation protocol enables:

- Consideration of robustness to H&E staining for CPath **model selection**
- Gaining insights into **individual model response** to different H&E staining conditions

Highlights

A protocol for evaluating robustness to H&E staining variation in computational pathology models

Lydia A. Schoenpflug, Nikki van den Berg, Sonali Andani, Nanda Horeweg, Jurriaan Barkey Wolf, Tjalling Bosse, Viktor H. Koelzer, Maxime W. Lafarge

- Evaluation protocol quantifies CPath model robustness to H&E staining variation
- Built a reference library of H&E stain properties from the PLISM dataset
- 306 CRC MSI classification models evaluated under four H&E staining conditions
- Robustness to staining variation is a key criterion for CPath model selection

A protocol for evaluating robustness to H&E staining variation in computational pathology models

Lydia A. Schoenpflug^{a,b}, Nikki van den Berg^c, Sonali Andani^{a,b}, Nanda Horeweg^d, Jurriaan Barkey Wolf^c, Tjalling Bosse^c, Viktor H. Koelzer^{a,b,*,1} and Maxime W. Lafarge^{a,b,1}

^aDepartment of Biomedical Engineering, University of Basel, Allschwil, Switzerland

^bInstitute of Medical Genetics and Pathology, University Hospital Basel, Basel, Switzerland

^cDepartment of Pathology, Leiden University Medical Center, Leiden, The Netherlands

^dDepartment of Radiation Oncology, Leiden University Medical Center, Leiden, The Netherlands

ARTICLE INFO

Keywords:

Computational pathology
Quality control
Domain generalization
H&E staining
Microsatellite instability

ABSTRACT

Sensitivity to staining variation remains a major barrier to deploying computational pathology (CPath) models as hematoxylin and eosin (H&E) staining varies across laboratories, requiring systematic assessment of how this variability affects model prediction. In this work, we developed a three-step protocol for evaluating robustness to H&E staining variation in CPath models. Step 1: Select reference staining conditions, Step 2: Characterize test set staining properties, Step 3: Apply CPath model(s) under simulated reference staining conditions. Here, we first created a new reference staining library based on the PLISM dataset. As an exemplary use case, we applied the protocol to assess the robustness properties of 306 microsatellite instability (MSI) classification models on the unseen SurGen colorectal cancer dataset (n=738), including 300 attention-based multiple instance learning models trained on the TCGA-COAD/READ datasets across three feature extractors (UNI2-h, H-Optimus-1, Virchow2), alongside six public MSI classification models. Classification performance was measured as AUC, and robustness as the min-max AUC range across four simulated staining conditions (low/high H&E intensity, low/high H&E color similarity). Across models and staining conditions, classification performance ranged from AUC 0.769-0.911 ($\Delta = 0.142$). Robustness ranged from 0.007-0.079 ($\Delta = 0.072$), and showed a weak inverse correlation with classification performance (Pearson $r = -0.22$, 95% CI [-0.34, -0.11]). Thus, we show that the proposed evaluation protocol enables robustness-informed CPath model selection and provides insight into performance shifts across H&E staining conditions, supporting the identification of operational ranges for reliable model deployment. The reference library and code are publicly available at <https://huggingface.co/datasets/CTPLab-DBE-UniBas/staining-robustness-evaluation> and <https://github.com/CTPLab/staining-robustness-evaluation>.

1. Introduction

Hematoxylin and eosin (H&E) staining is central to diagnostic histopathology and forms the input of most computational pathology (CPath) pipelines. However, the appearance of Whole Slide Images (WSIs) of H&E-stained specimens exhibits substantial variability within and across laboratories due to differences in staining protocols, reagent concentrations, batch effects, scanner characteristics, and tissue processing workflows Dunn et al. (2025). These differences produce shifts in stain intensity, color, and can alter morphological information, which can affect model performance when CPath models are applied to WSIs of specimens prepared at different timepoints or institutions Folsmbe et al. (2019); Howard et al. (2021); Lin et al. (2025a); Stacke et al. (2021); Tellez et al. (2019).

*Corresponding author

 vikt.or.koelzer@usb.ch (V.H. Koelzer)

ORCID(s): 0009-0009-6703-9368 (L.A. Schoenpflug);

0009-0003-2567-5311 (N.v.d. Berg); 0000-0003-3251-5108 (S. Andani);

0000-0002-8581-4753 (N. Horeweg); 0000-0002-7811-0280 (J.B. Wolf);

0000-0002-6881-8437 (T. Bosse); 0000-0001-9206-4885 (V.H. Koelzer);

0000-0001-9235-783X (M.W. Lafarge)

¹These authors contributed equally as senior authors.

Prior work addressing staining-related domain shift can be broadly grouped into development-focused and evaluation-focused approaches. Development-focused methods, including stain normalization Macenko et al. (2009); Janowczyk et al. (2017); Sim (2025); Du et al. (2025), stain augmentation Balkenhol et al. (2018); Tellez et al. (2019); Bentaieb and Hamarneh (2018); Nishar et al. (2020); Shen et al. (2022); Marini et al. (2023), and domain-adversarial training Lafarge et al. (2017); Otálora et al. (2019), all aim to improve robustness during training. However, a critical gap arises in the context of modern computational pathology pipelines: existing methods primarily focus on improving encoder-level training, assuming encoders are trained locally. At the same time the field has shifted toward large pre-trained foundation models, whose training is restricted to institutions with access to massive datasets and computational resources (e.g. UNI: >100k WSIs, 32 GPUs) Xiong et al. (2025). As a result, most researchers no longer modify the encoder but instead train lightweight attention-based multiple instance learning (ABMIL) classifiers on top of features extracted by frozen foundation models, further referred to as two-stage training pipelines. In this setting, training-time strategies such as stain augmentation or normalization have reduced influence Wölfllein et al. (2025), as their impact is constrained by the pre-trained feature representations. At the same time, current foundation

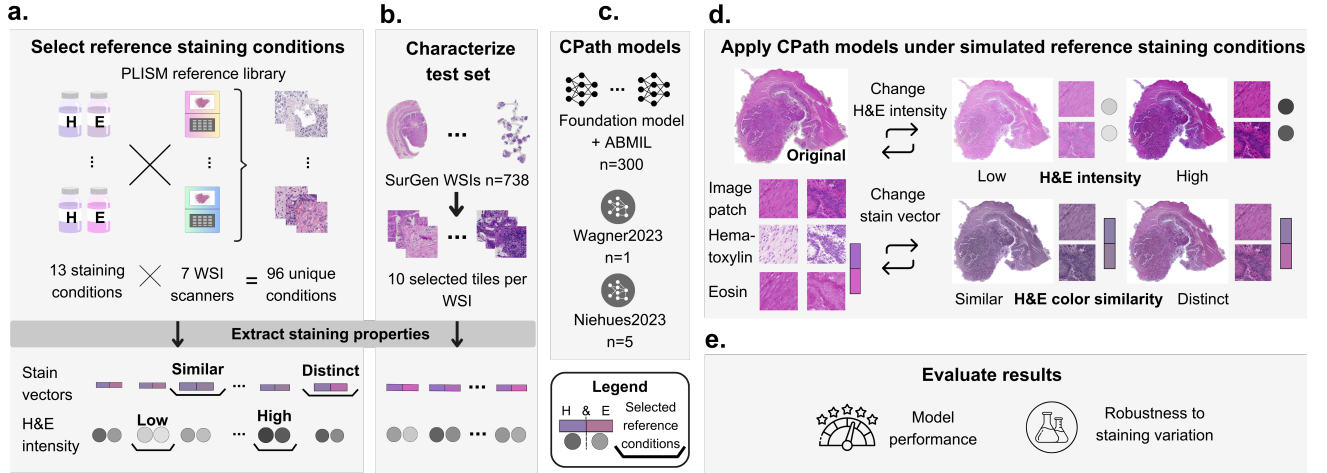


Figure 1: A protocol for evaluating robustness to staining variation of CPath models. a) Select reference staining conditions based on the reference library created from the PLISM dataset. b) Characterize SurGen test set staining properties. c) State-of-the-art MSI classification models, with $n=300$ models reflecting plausible state-of-the-art models which were trained on TCGA COADREAD using one of three foundation models as feature extractors (Uni2-h, HOptimus1, Virchow2) and ABMIL for aggregation. We also considered $n=6$ publicly available models. d) Infer MSI classification models under four simulated reference staining conditions. e) Evaluation of results by measuring model performance and robustness to staining variation.

models are not fully invariant to domain shifts, including staining variability: extracted features retain institution-specific information Lin et al. (2025b); de Jong et al. (2025); Kömen et al. (2024); Kömen et al. (2025). Yet, pipelines based on foundation models generally outperform previous approaches, suggesting that adequate pretraining confers a measurable improvement in robustness to staining variation and reduces, but does not eliminate, sensitivity to H&E variability. Evaluation-focused studies have demonstrated that staining variability can affect performance more strongly than many common artifacts Wang et al. (2021); Foote et al. (2022); Schömig-Markiefka et al. (2021); Vu et al. (2022). Yet, existing evaluation strategies often rely on image-based references Schömig-Markiefka et al. (2021); Vu et al. (2022), generative transformations Springenberg et al. (2023), fixed multiplier perturbations Wang et al. (2021), or re-staining/re-scanning protocols Miranda Ruiz et al. (2023); Sun et al. (2023); Chai et al. (2026), which make it difficult to attribute performance changes to specific, quantifiable staining properties or to situate perturbations within a defined staining reference space. Taken together, these observations highlight a need for systematic evaluation methods that quantify the robustness to staining variation of trained two-stage CPath pipelines at inference time, while anchoring perturbations to defined staining properties. Such methods can inform both model selection and diagnostic slide preparation, supporting data-driven quality control.

To address this deficit, we introduce a protocol for systematically evaluating the robustness of computational pathology models under realistic H&E staining variations (Figure 1). Our approach simulates plausible staining conditions while preserving tissue structure, thereby enabling quantitative assessment of model robustness. We demonstrate this protocol using microsatellite instability (MSI)

classification in colorectal cancer, evaluating multiple state-of-the-art models and providing a methodological basis for evidence-based slide preparation and quality control in clinical workflows.

2. Methods

2.1. Stain decomposition and controlled recomposition framework

We modeled the RGB pixel intensities of a histology image $I \in [0, 255]^{H \times W \times 3}$ as a function of the optical density (OD) using the Beer-Lambert law

$$\text{OD} = -\log\left(\frac{I}{I_0}\right), \quad (1)$$

where I_0 denotes the illumination constant (typically 255). Following Macenko et al. (2009), the OD of each pixel is assumed to lie in the subspace spanned by the hematoxylin and eosin stain vectors $\mathbf{s}_H, \mathbf{s}_E \in \mathbb{R}^3$. We further include a third residual vector \mathbf{s}_R orthogonal to the H&E plane to account for residual variation. Using this framework, each pixel's optical density is represented as

$$\text{OD} \approx i_H \mathbf{s}_H + i_E \mathbf{s}_E + i_R \mathbf{s}_R, \quad (2)$$

where $i_H, i_E, i_R \geq 0$ denote the stain intensities, quantifying the per-pixel staining magnitude. For image-level quantification, the H&E stain intensity is defined as the 95th percentile across all pixels. To robustly identify the H&E stain vectors, the OD matrix of filtered pixels is analyzed via singular value decomposition. The two dominant singular vectors define the H&E plane, in which the stain vectors are subsequently identified, and the third singular vector defines the residual vector. Pixels with extreme OD values are excluded to avoid

artifacts. For staining simulations, OD projections are scaled to target H&E intensities and recombined using the target stain vectors, with the residual component reduced by a factor of 0.01 to minimize its effect.

2.2. Datasets

2.2.1. PLISM

The Pathology Images of Scanners and Mobilephones (PLISM) dataset Ochi et al. (2024) comprises aligned image patches from 46 human tissue types, stained under 13 H&E staining conditions and digitized using 13 imaging devices, with recorded slide preparation parameters¹. This design enables extraction of realistic H&E staining intensities and stain vectors for downstream simulation. As this study is focused on the analysis of WSIs, we restricted the analysis to the subset of images patches of the PLISM dataset captured with WSI scanners (PLISM-wsi). The final subset includes 310,947 patches, corresponding to 3,417 aligned patches across 91 unique stain-device combinations (Appendix Table A.1 and A.2). We excluded the HR and GIV staining conditions for our study, as we consider the overnight hematoxylin exposure to produce an unrealistically intense staining.

2.2.2. TCGA COAD/READ

The TCGA Colon and Rectum Adenocarcinoma cohorts (COAD, READ) were used as the development set for training and validating a set of plausible “black-box” MSI classifiers. A total of 625 diagnostic WSIs of H&E-stained formalin-fixed paraffin-embedded (FFPE) resection specimens from 616 patients were downloaded from the Genomic Data Commons portal² of which 25 WSIs were excluded due to file corruption, yielding 600 WSIs from 591 patients. MSI status was obtained for all patients from two sources available through cBioPortal³: (i) the PanCancer Atlas Bonneville et al. (2017), providing next-generation sequencing (NGS)-derived MSI calls using MANTIS Kautto et al. (2016), and (ii) the original TCGA publications Network (2012) which reported PCR-based MSI status. When both labels were available, NGS-derived MSI calls were prioritized to ensure a consistent, genome-wide reference standard across the cohort.

2.2.3. SurGen

The SurGen dataset Myles et al. (2025) is a publicly available⁴ collection of WSIs of FFPE H&E-stained CRC resection and biopsy specimens and was used solely as a hold-out test set in this study. It comprises 1,020 WSIs from 843 patients and is divided into two subsets: SR386, containing primary colorectal tumors with matched genomic and clinical annotations, and SR1482, which includes both primary and metastatic cases. MSI status was derived from either

¹<https://huggingface.co/datasets/owkin/plism-dataset-tiles>, last accessed 04.12.2025.

²<https://portal.gdc.cancer.gov/>, last accessed 04.12.2025.

³<https://www.cbioportal.org/>, last accessed 04.12.2025.

⁴<https://www.ebi.ac.uk/biostudies/bioimages/studies/S-BIAD1285>, last accessed 04.12.2025.

PCR-based fragment analysis or mismatch-repair (MMR) immunohistochemistry (IHC), with PCR-based calls preferred where available. For IHC-derived labels, loss of expression of one or more MMR proteins was interpreted as microsatellite instable, intact expression of all MMR proteins was interpreted as microsatellite stable. Patients with WSIs exclusively from non-colorectal metastatic sites (n=92), missing MSI status (n=11), or providing insufficient tissue (n=2) were excluded, resulting in 738 patients with 892 WSIs. When multiple slides were available for the same patient, the first available WSI was selected.

2.3. Models

2.3.1. Simulated models

To reflect the diversity of models that may realistically be developed or received by clinical implementers, we simulated a set of ABMIL models trained on TCGA COAD/READ using foundation-model-based pipelines. Tissue detection was performed on all WSIs using the tissue segmentation model of Bándi et al. (2019), followed by tiling into 224×224 px patches at $1\mu\text{m}/\text{px}$ for feature extraction. No stain augmentation or normalization was applied, following established ABMIL training frameworks Wölflein et al. (2025). To induce realistic variability, we sampled across multiple hyperparameters: three foundation model feature extractors (UNI2-h⁵ Chen et al. (2024), H-Optimus-1⁶ Bioptimus (2025), Virchow2⁷ Zimmermann et al. (2024)) with 100 models per extractor, arbitrary random initialization seeds, two weight decay values (0 or 10^{-4}), MSI-stratified 70:30 patient-level train-validation splits with or without institutional overlap, and random exclusion of 0–10 institutions per model while retaining at least 90% of the development dataset. This approach simulates variability in data splits, training methodology, and institutional coverage. Slide-level aggregation of patch-level features was performed using a gated ABMIL model adapted from Lu et al. (2021), with an additional pre-compression fully connected layer. Models were trained using AdamW Loshchilov and Hutter (2019) with learning rate $5 \cdot 10^{-5}$, momentum 0.95/0.999, cosine annealing, batch size 1, early stopping with five-epoch patience based on validation AUC, and a maximum of 30 epochs.

2.3.2. Public models

In addition to the simulated models, we included six publicly available, trained MSI classification models from two publications. The first, Wagner2023 Wagner et al. (2023), uses the CTransPath Wang et al. (2022) model for feature extraction from 512×512 px image patches at $0.5\mu\text{m}/\text{px}$ (resized to 224×224 px, $1.14\mu\text{m}/\text{px}$), followed by a transformer-based MIL (TransMIL) aggregator. The TransMIL model was trained on WSIs from over 13,000 CRC patients across 16 cohorts. The five other models, Niehues2023 Niehues et al. (2023), use the RetCCL Wang et al. (2023) model for

⁵<https://huggingface.co/MahmoodLab/UNI2-h>, last accessed 04.12.2025.

⁶<https://huggingface.co/bioptimus/H-Optimus-1>, last accessed 04.12.2025.

⁷<https://huggingface.co/paige-ai/Virchow2>, last accessed 04.12.2025.

feature extraction with identical input format as Wagner2023 (224 × 224px, 1.14µm/px) and gated ABMIL aggregation. These five models were trained with different dataset splits under a 5-fold cross-validation framework. Feature extractors and pretrained MIL weights were obtained from the authors' publicly released repositories⁸. Inference was performed without stain normalization and consisted of feature extraction using CTransPath or RetCCL, followed by aggregation with the respective pretrained MIL models to obtain slide-level MSI classifications.

2.4. Protocol for evaluating robustness to H&E staining variation

Our protocol for evaluation of CPath model robustness to H&E staining variation comprises three stages. First, reference staining conditions are selected based on a reference library. Here, we first created a new reference library from the PLISM dataset. Second, the test set staining properties are characterized, specifically slide-wise stain vectors and intensities are extracted. Third, inference of the CPath model is performed under a controlled set of simulated staining conditions. Here, we present the application of this protocol to MSI classification models, evaluated and compared using the holdout SurGen test set.

2.4.1. Step 1: Select reference staining conditions

To enable reference selection we first created a new reference library from the PLISM dataset. Only tiles meeting quality criteria (Appendix Table B.1) were included. Stain vectors and intensities were extracted for these tiles as described in section 2.1, and median values across tiles were computed for each stain-device combination to define representative H&E stain vectors and intensities. Stain intensity was quantified as the 95th percentile of hematoxylin and eosin intensities in the stain-separated projections, capturing well-stained tissue while avoiding extreme artifacts (e.g., blood). For simulating intensity-based changes, the conditions with lowest and highest H&E intensity were selected. To simulate changes of H&E stain colors, we selected stain vector references reflecting common diagnostic hematoxylin formulations: Harris for the most distinct and Gill for the most similar H&E stain colors, where similarity was measured as the angle between H&E vectors in OD space. These references enable realistic simulation of both intensity- and color-based variations in H&E staining. Exemplary tiles and staining details for each reference can be found in Appendix Figure B.1 and Table B.2. All the stain vectors and intensities derived from the PLISM dataset were released as a public reference library⁹.

⁸CTransPath: <https://huggingface.co/jamesdolezal/CTransPath>; RetCCL: <https://github.com/Xiyue-Wang/RetCCL>; Wagner2023: <https://github.com/peng-lab/HistoBistro/tree/main/CancerCellCRCTransformer>; Niehues2023: https://github.com/KatherLab/crc-models-2022/tree/main/Quasar_models/Wang%2BattMIL/isMSIH; all last accessed 15.01.2026.

⁹PLISM stain references on HuggingFace: https://huggingface.co/datasets/CTPLab-DBE-UniBas/staining-robustness-evaluation/tree/main/plism-wsi_stain_references

2.4.2. Step 2: Characterize test set staining properties

For each slide of the SurGen dataset, slide-level stain vectors and H&E intensities were obtained by sampling 10 tiles (448px × 448px at 0.5µm/px) per slide that passed the tile quality criteria (Appendix Table B.1). In rare cases where artifact colors affected decomposition (e.g. pink, orange, brown, or dark-red blood), quality criteria were manually adjusted until visual review of the derived stain vectors showed alignment with WSI stain appearance. Stain vectors and H&E intensity values were extracted as described for the PLISM reference conditions, and slide-level representatives were computed as the median across the sampled tiles. Slide-wise stain intensities and vectors then served as the basis for staining simulations during inference. All the slide-level stain vectors and intensities were made publicly available¹⁰.

2.4.3. Step 3: Apply CPath model under simulated reference staining conditions

Inference under controlled, simulated staining conditions on SurGen WSIs consisted of tissue detection with the tissue segmentation model of Bándi et al. (2019), followed by tiling into patches, matching the input size and resolution of the respective feature extractor as specified in section 2.3.1 and 2.3.2. Tiles are then decomposed into hematoxylin and eosin channels using the slides' stain vectors, and are further recomposed based on the target PLISM references to simulate the target staining conditions as described in section 2.1. Experiments covered four PLISM-defined conditions: low vs. high H&E intensity and high vs. low H&E color similarity. In the intensity conditions, only stain intensities were varied (stain vectors fixed), whereas in the color similarity conditions only stain vectors were varied (intensities fixed). Features were extracted once for all foundation models and conditions.

2.5. Evaluation metrics

Model performance was quantified as the AUC on the reference staining condition, and robustness to staining variation as the min-max range of AUCs across the five staining conditions (reference and four simulated staining conditions). Models were considered high-performing with a reference AUC over 90% and highly robust with a min-max AUC range of less than 3%. Confidence intervals were estimated using 1,000 bootstrap resamples of the SurGen cohort. For each iteration, AUCs were computed for all five conditions, yielding a bootstrap-specific min-max range (robustness) and reference AUC (performance). To compare performance between the reference and simulated staining conditions, we calculated the difference in AUC (Δ AUC). Distribution and variability of Δ AUCs were summarized using median, quantile and minimum statistics. Further, staining conditions were ranked by AUC for each model, and we recorded how many models achieved their highest AUC under each condition. For visualization purposes,

¹⁰SurGen stain references on HuggingFace: https://huggingface.co/datasets/CTPLab-DBE-UniBas/staining-robustness-evaluation/tree/main/surgen_stain_properties

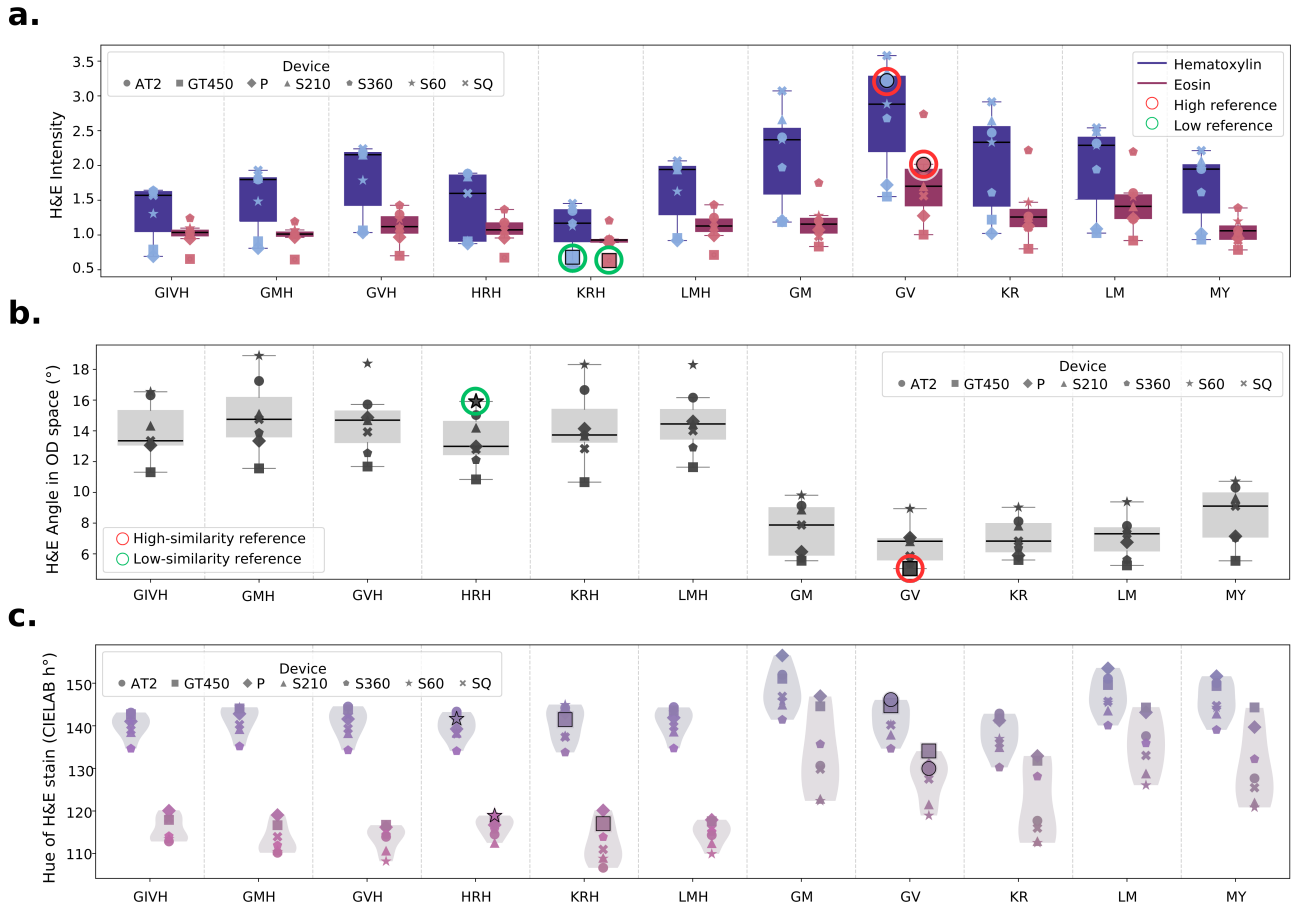


Figure 2: Staining characteristics of PLISM staining condition-device combinations. a) Intensity of Hematoxylin and Eosin, b) Angle between H&E stain vector in OD space, c) Distribution of H&E hues, measured as hue h° in CIELab space; left violin: Hematoxylin, right violin: Eosin. Marker colors correspond to RGB stain colors. The selected reference conditions (low and high intensity; low and high H&E color similarity) are circled in red and green respectively and highlighted with a black frame. For staining condition and device abbreviations please refer to Appendix Table A.1 and A.2.

staining characteristics were summarized using stain intensity, stain similarity as the angle between H&E vectors in OD space, and stain hue quantified as the hue angle ($h^\circ = \arctan 2(b^*, a^*)$) in CIELab space.

2.6. GPU Usage and Code availability

All code was implemented in Python, model training and inference was done with PyTorch. Training and inference were performed on NVIDIA H200 GPUs, totaling 444 GPU hours. Energy usage was measured via nvidia-smi and totaled 208.45 kWh (Appendix Table C.1). Code for stain vector and intensity extraction, model training, inference, analysis, and visualization is publicly available on GitHub¹¹. We further make PLISM and SurGen stain vectors and intensities, all 300 trained models and experiment results publicly available¹².

¹¹GitHub Repository: <https://github.com/CTPLab/staining-robustness-evaluation/tree/main>

¹²HuggingFace Repository: <https://huggingface.co/datasets/CTPLab-DBE-UniBas/staining-robustness-evaluation/tree/main>

3. Results

3.1. PLISM-derived stain and intensity references

To establish a benchmark for realistic H&E staining changes, we first characterized the H&E intensities and stain vectors for each unique PLISM stain-device condition. Consistent with the PLISM study design, conditions intended to be more distinct in H&E color (ending with “H”) showed larger angles between H&E stain vectors compared to similar H&E color conditions (Figure 2a+b). This pattern was also reflected in H&E hues, which displayed greater separation for distinct stain color conditions (Figure 2c). Furthermore, we note that PLISM conditions optimized for distinct H&E colors exhibited lower H&E intensities compared to higher similarity conditions (median H: 1.58 vs 2.10; median E: 1.04 vs 1.35). This difference did not map consistently onto a single recorded slide preparation parameter (e.g., hematoxylin formulation, exposure duration, or number of dehydration steps), suggesting a multifactorial relationship. Hematoxylin intensity varied more across staining conditions than across WSI scanners (mean

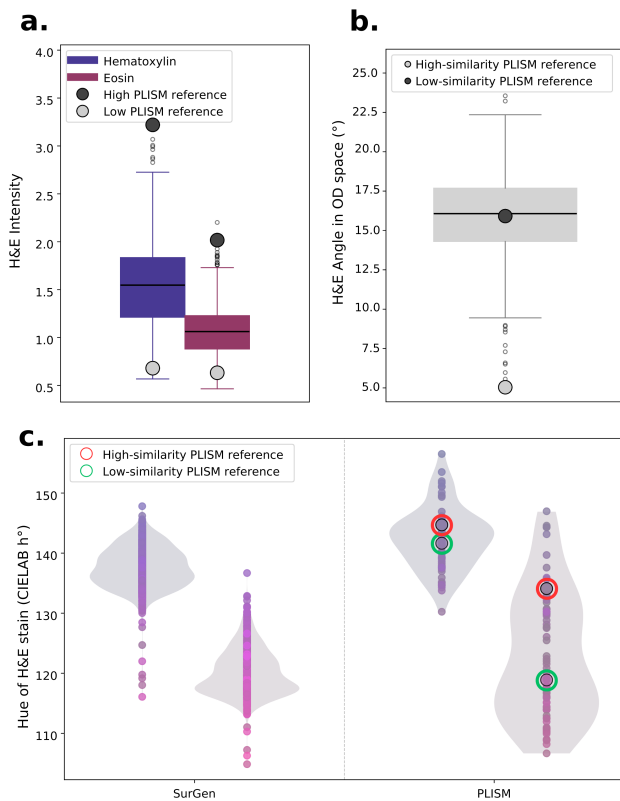


Figure 3: Staining characteristics of SurGen WSIs. a) Intensity of Hematoxylin and Eosin, b) Angle between H&E stain vector in OD space, c) Distribution of H&E hues, measured as hue h° in CIE Lab space; left violin: Hematoxylin, right violin: Eosin. Marker colors correspond to RGB stain colors; low and high color similarity PLISM references are circled in green and red respectively.

std across stains = 0.56 vs. across devices = 0.47). In contrast, stain similarity and Eosin intensity was impacted more strongly by WSI scanning effects, with higher standard deviation across devices than across stainings (H&E stain angle mean std across devices = 3.7° vs. across stainings = 1.9° ; Eosin intensity mean std across stainings = 0.28 vs. across devices = 0.25).

3.2. Distribution of H&E staining intensity and colors in the SurGen dataset

Analysis of SurGen slide-level H&E intensities and stain vectors revealed substantial intrinsic variability, encompassing, and in some cases, exceeding the selected PLISM reference conditions (Figure 3). Hematoxylin and eosin intensities ranged from 0.57-3.10 and 0.46-2.20, slightly extending beyond the low ($H = 0.68$, $E = 0.63$) and high ($H = 3.22$, $E = 2.02$) PLISM reference intensities. H&E hues also marginally extended the PLISM reference range. H&E stain color similarity, measured as the angle between H&E vectors, spanned 5.1° - 23.6° , covering the PLISM “high-similarity” reference (5.0°) and surpassing the “low-similarity” reference (15.9°).

3.3. Robustness-performance relationship in MSI classification

To examine how model performance relates to robustness under staining simulations, we evaluated model performance on the SurGen dataset under the original and four simulated H&E staining conditions for the 306 MSI classification models. Across all models, reference performance ranged from AUC 0.769-0.911, robustness to staining variation ranged from 0.007-0.079 and exhibited a weak inverse association ($r = -0.28$, 95% CI = [-0.39, -0.17], $n = 306$), indicating that higher reference AUC does not necessarily imply greater robustness to staining variability (Figure 4a). However, this varied depending on the foundation model. A moderate negative correlation was observed for UNI2-h+ABMIL ($r = -0.51$, 95% CI = [-0.63, -0.39], $n = 100$) and Virchow2+ABMIL ($r = -0.36$, 95% CI = [-0.52, -0.19], $n=100$), while no significant association was observed for H-Optimus-1+ABMIL ($r = -0.14$, 95% CI = [-0.36, 0.10], $n = 100$) and the RetCCL+Niehu2023 models ($r = -0.75$, no 95% CI due to low sample size, $n = 5$). Reference AUC distributions across foundation models are summarized in Appendix D, showing differences in median performance (median AUC UNI2-h: 0.881, H-Optimus-1: 0.865, Virchow2: 0.856, across $N=100$ models), but substantial overlap in interquartile ranges (UNI2-h: [0.860, 0.892], H-Optimus-1: [0.848, 0.878], Virchow2: [0.838, 0.873]).

Considering only the high-performing, highly robust models ($n=10$), predominantly UNI2-h+ABMIL models, alongside the CTransPath+Wagner2023 model and two H-Optimus-1+ABMIL models remained (Figure 4b). Among these, reference performance was very similar: the top-performing CTransPath+Wagner2023 model achieved an AUC of 0.911, closely followed by UNI2-h+ABMIL models (0.902-0.911), and slightly lower-performing H-Optimus-1+ABMIL models (0.902-0.905). In contrast, robustness differed more clearly across models: UNI2-h+ABMIL models showed consistently smaller robustness ranges (0.009-0.013) than H-Optimus-1+ABMIL (0.020-0.024) and CTransPath+Wagner2023 (0.021). Bootstrap analysis reinforced this separation: whereas 95% confidence intervals (CIs) for reference AUC largely overlapped across top-performing models (Figure 4b, CTransPath+Wagner2023: [0.869,0.950]; best UNI2-h+ABMIL: [0.875,0.944]; best H-Optimus-1+ABMIL: [0.865,0.941]), robustness CIs were narrower and more discriminative. Median robustness CI width was smallest for UNI2-h+ABMIL (0.019), compared with H-Optimus-1+ABMIL (0.031) and CTransPath+Wagner2023 (0.030), indicating greater stability.

3.4. Impact of staining conditions on model performance

Finally, we assessed how each of the four simulated staining conditions influenced model performance compared to the reference. Across all models ($n=306$), the high intensity condition most frequently yielded the highest AUC (127 models), followed by low H&E color similarity (51 models), whereas the reference condition was optimal in

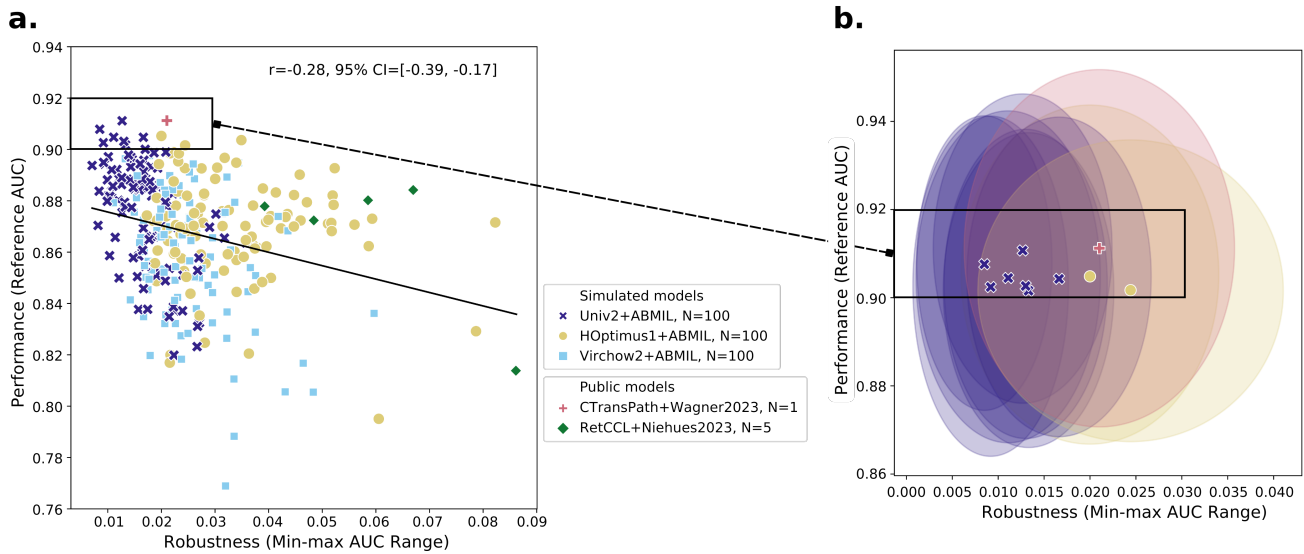


Figure 4: Performance-robustness relationship across MSI classification models: a) Performance (AUC of reference condition) versus robustness (min-max AUC across all stain conditions) for all evaluated models ($n=306$). We report Pearson correlation between performance and robustness with 95% CIs. b) Top models (Performance > 0.90 , Robustness < 0.03 ; $n=10$). Dots indicate bootstrapped means ($n=1000$ iterations); ellipses represent 95% CIs for both performance and robustness.

Table 1

Effects of simulated H&E staining conditions on all models ($n = 306$) and top-performing, robust models ($n = 10$). For each condition, the table reports the number of models for which it performed best, the median Δ AUC relative to reference with 95% CI, and the worst-case AUC decrease compared to reference.

All models ($n=306$)			
Staining Condition	Best model count	Median Δ AUC [95% CI]	Worst-case AUC decrease
Reference	65	-	-
Low intensity	30	-0.50% [-1.13%, -0.05%]	-4.50%
High intensity	127	0.12% [-0.65%, 0.73%]	-4.36%
Low H&E color similarity	51	-0.07% [-0.52%, 0.34%]	-3.17%
High H&E color similarity	33	-0.57% [-1.57%, 0.11%]	-7.78%
Top models ($n=10$)			
Staining Condition	Best model count	Median Δ AUC [95% CI]	Worst-case AUC decrease
Reference	0	-	-
Low intensity	0	-0.46% [-0.63%, -0.07%]	-1.08%
High intensity	8	0.50% [0.36%, 0.73%]	-0.37%
Low H&E color similarity	2	0.24% [0.05%, 0.39%]	-0.20%
High H&E color similarity	0	-0.32% [-0.62%, -0.02%]	-1.87%

65 models (Table 1). At the same time, each condition was associated with performance decreases in subsets of models, with worst-case scenarios of more than 3% performance decrease for any condition (Table 1). Restricting to high-performing, robust models ($n=10$), high intensity remained the most favorable condition (8/10 models, median Δ AUC +0.50%, Table 1, Appendix Figure E.1a), achieving the overall highest AUCs on the SurGen dataset for the CTransPath+Wagner2023 model and a single H-Optimus-1+ABMIL model (both: 0.920), exceeding their respective reference-condition performance (CTransPath+Wagner2023: 0.911, H-Optimus-1+ABMIL: 0.904). Simultaneously, low intensity and high H&E color similarity led

to modest median decreases (-0.46% and -0.32%, Table 1, Appendix Figure E.1b). Worst-case AUC drops also followed a condition-dependent pattern: decreases were minimal ($< 0.4\%$) for high intensity and distinct H&E color conditions, but larger ($> 1\%$) for low intensity and similar H&E color conditions.

4. Discussion

This study provides an evaluation protocol to 1) quantify the robustness of computational pathology models to H&E staining variability and to 2) systematically assess how staining conditions affect model performance. Across

a large population of MSI classification models, we observed substantial heterogeneity in robustness against staining variability, with only a weak inverse relationship between performance and robustness. This suggests that higher predictive performance does not guarantee stability under staining shifts, supporting the notion that robustness to staining variation is a partially independent property of trained models Lin et al. (2025a); Stacke et al. (2021). Notably, we found that this pattern persists even in foundation-model-based pipelines, and becomes particularly evident when evaluating many downstream predictors under simulated staining conditions, rather than focusing on a single best-performing model. Unexpectedly, UNI2-h and H-Optimus-1 foundation models were found to be more robust than Virchow2, contrasting prior reports de Jong et al. (2025); Kömen et al. (2025). Furthermore, the Wagner2023 model, though built on the less robust CTransPath foundation model Kömen et al. (2025), ranked among the top three in both performance and robustness to staining variation, suggesting that aggregator training can mitigate foundation model sensitivity to staining variability. Overall, we found that high-performing, robust models exist and can be identified by considering both metrics jointly. Systematic trends in model performance emerged across staining conditions. Across all models, high intensity and low H&E color similarity conditions more frequently yielded top performance, whereas low intensity and high H&E color similarity tended to produce slightly negative shifts relative to the reference. However, these effects were not universal, as all conditions produced the best AUCs for subsets of models. Considering only high-performing, robust models, the same patterns were more pronounced: high intensity and low H&E color similarity most often corresponded to the highest AUCs, while low intensity and high H&E color similarity produced modest decreases. Nonetheless, individual models continued to deviate from these trends, indicating that the effect of staining conditions remains model-dependent and should be assessed individually. Further, our analysis adds a key piece in understanding the origin of staining variability: in the PLISM dataset hematoxylin intensity was mainly driven by the 13 staining protocols, while stain color similarity and eosin intensity were more strongly influenced by the scanner choice out of seven devices. Since scanners are often fixed, whereas staining protocols can be more easily adjusted, identifying staining conditions that perform reliably with the scanners in use is crucial. The observed H&E staining properties of slides under the same staining protocol may change depending on the scanner, highlighting the need to validate both the staining workflow and its interaction with the lab's scanners to ensure robust model performance.

Prior work on evaluating CPath model robustness to staining variation has focused on using image-based references Schömig-Markiefka et al. (2021); Vu et al. (2022), generative Springenberg et al. (2023), or physically repeated staining protocols Chai et al. (2026); Sun et al. (2023); Miranda Ruiz et al. (2023). While establishing the clinical

relevance of staining variability, they do not anchor perturbations to quantifiable stain intensities or similarity measures within a defined reference space. Consequently, attribution of performance changes to specific staining properties remains challenging. In contrast, our protocol applies deterministic, reference-based staining simulations that explicitly control stain intensity and similarity, enabling systematic testing of trained models under defined staining conditions. This enables interpretable assessment of robustness to staining variation and provides a structured, reference-based evaluation protocol that complements existing training- and evaluation-focused approaches.

Our study has several limitations. First, the PLISM reference library captures only part of the staining variability observed in clinical slides, with the SurGen cohort often exceeding its range for H&E stain angles, indicating that capturing additional stain preparation protocols and scanner combinations would be beneficial. While larger reference sets with pre-extracted stains exist Marini et al. (2023), they do not allow verification of color correctness, lack intensity properties as well as traceable diagnostic conditions. PLISM, in contrast, provides known staining properties and scanner origins across a broad range of tissue types. Second, this protocol is focused on staining properties only and does not systematically assess other QC factors such as tissue folds, blur or air bubbles, or scanner-induced effects on sharpness and image quality. However, prior work shows that staining is among the strongest factors influencing model performance Wang et al. (2021); Foote et al. (2022); Schömig-Markiefka et al. (2021); Vu et al. (2022). Third, the protocol currently only models H&E staining properties in standard tissue regions. Other components on the slide, such as blood, necrosis, or heavily pigmented areas, behave differently under staining variation and when acquired with different scanners and would require more sophisticated unmixing methods for accurate modeling. Lastly, only four discrete staining conditions were tested, limiting exploration of continuous or non-linear effects.

5. Conclusion

We present a protocol for systematically quantifying the robustness to H&E staining variation of computational pathology models, revealing how specific H&E staining properties impact performance across a broad set of MSI classification models. Our analysis suggests that robustness to H&E staining variation is a model-specific property, only partially correlating with overall predictive performance, and highlights the interplay between staining protocols and scanner choice in shaping digital appearance. Staining conditions produced trends in model performance: in our experiments, high intensity was associated with slightly better performance, while low intensity or highly similar H&E colors tended to cause modest decreases. However, this was not universal, with subsets of models showing reverse effects, highlighting the need for model-specific evaluation. These results demonstrate that the proposed protocol can serve as

a universal stress-testing tool, revealing both general trends and model-specific sensitivities, and providing actionable guidance for robust deployment of CPath models.

Our findings highlight actionable directions for both clinical implementers and algorithm developers in advancing stain-robust computational pathology. For clinical implementers, we recommend characterizing the staining properties of routine WSIs, including H&E intensity and stain vectors, over time. Continuous monitoring via QC protocols can identify operational ranges and outliers, enabling targeted re-staining or re-scanning. Local validation sets can be built from observed slides or by simulating stains at the edges of these operational ranges using protocols like ours, helping ensure consistent laboratory output and robust deployed models within expected staining changes. For algorithm developers, creating reference libraries that capture realistic, traceable, and institution-relevant staining conditions is critical. Public datasets often lack intensity information or include unrealistic color variations, limiting their utility for QC. Combining publicly available references with locally characterized staining properties enables defining operational ranges in which models perform reliably. Ideally, standardized reference sets could be harmonized across institutions and countries to define minimal “fit for purpose” robustness requirements for CPath models, supporting domain generalization, regulatory confidence, and trust in clinical deployment. Future work should extend robustness evaluation beyond rank-based discriminative performance to include absolute score stability, calibration shifts, and scaling drifts under staining changes. Expanding these analyses to other tasks, modalities (e.g. IHC), and systematically studying interactions between staining, scanning, and training strategies would provide a more complete understanding of model sensitivity and guide both algorithm development and clinical quality assurance, supporting reliable and generalizable deployment of CPath models.

Acknowledgments

The results published here are in whole or part based upon data generated by the TCGA Research Network: <https://www.cancer.gov/tcga>. We thank all the patients who contributed samples to the SurGen study and TCGA, enabling this research.

Declaration of competing interest

L.S. reports travel reimbursement for participation as an invited speaker for Indica Labs. T.B and N.H. received research funding from the Dutch Cancer Society. T.B is supported by the Hanarth Fund, unrelated to the present study. V.K. is a participant in several patent applications on the assessment of cancer biomarkers by digital pathology. T.B., V.K. and N.H. are participants on a patent application on multimodal deep learning for the prediction of recurrence risk in endometrial cancer patients. V.K. reports sponsored research agreements with Roche and IAG, honoraria or consulting fees from Takeda and Roche, and participation

as an invited speaker for Sharing Progress in Cancer Care and Indica Labs, all unrelated to the present study. The other authors declare no competing interests.

Declaration of generative AI and AI-assisted technologies in the manuscript preparation process

During the preparation of this work the authors used ChatGPT in order to structure and polish the text. After using this tool, the authors reviewed and edited the content as needed and take full responsibility for the content of the published article.

Funding

This research did not receive any specific grant from funding agencies in the public, commercial, or not-for-profit sectors.

CRedit authorship contribution statement

Lydia A. Schoenpflug: Conceptualization, Data curation, Formal analysis, Investigation, Methodology, Project administration, Software, Validation, Visualization, Writing - Original Draft, Writing - Review & Editing. **Nikki van den Berg:** Conceptualization, Writing - Review & Editing. **Sonali Andani:** Conceptualization, Writing - Review & Editing. **Nanda Horeweg:** Conceptualization, Supervision, Writing - Review & Editing. **Jurriaan Barkey Wolf:** Software, Writing - Review & Editing. **Tjalling Bosse:** Conceptualization, Writing - Review & Editing. **Viktor H. Koelzer:** Conceptualization, Funding acquisition, Supervision, Writing - Review & Editing. **Maxime W. Lafarge:** Conceptualization, Methodology, Project administration, Software, Supervision, Writing - Review & Editing.

References

- Balkenhol, M., Karssemeijer, N., Litjens, G.J.S., van der Laak, J., Ciompi, F., Tellez, D., 2018. H&E stain augmentation improves generalization of convolutional networks for histopathological mitosis detection, in: *Medical Imaging 2018: Digital Pathology*, SPIE. p. 34. URL: <https://doi.org/10.1117/12.2293048>, doi:10.1117/12.2293048.
- Bentaieb, A., Hamarneh, G., 2018. Adversarial stain transfer for histopathology image analysis. *IEEE Transactions on Medical Imaging* 37, 792–802. doi:10.1109/TMI.2017.2781228.
- Bioptimus, 2025. H-optimus-1. <https://huggingface.co/bioptimus/H-optimus-1>. [Software, version 1.0].
- Bonneville, R., Krook, M.A., Kautto, E.A., Miya, J., Wing, M.R., Chen, H.Z., Reeser, J.W., Yu, L., Roychowdhury, S., 2017. Landscape of microsatellite instability across 39 cancer types. *JCO Precision Oncology*, 1–15 URL: <https://ascopubs.org/doi/abs/10.1200/P0.17.00073>, doi:10.1200/P0.17.00073, arXiv:<https://ascopubs.org/doi/pdf/10.1200/P0.17.00073>. PMID: .
- Bándi, P., Balkenhol, M., van Ginneken, B., van der Laak, J., Litjens, G., 2019. Resolution-agnostic tissue segmentation in whole-slide histopathology images with convolutional neural networks. *PeerJ* 7, e8242. URL: <https://doi.org/10.7717/peerj.8242>, doi:10.7717/peerj.8242.

- Chai, B., Chen, J., Cool, P., Oumlil, F., Tollitt, A., Steiner, D.F., Chakraborti, T., Flanagan, A.M., 2026. Impact of tissue staining and scanner variation on the performance of pathology foundation models: a study of sarcomas and their mimics. *The Journal of Pathology: Clinical Research* 12, e70080. URL: <https://pathsocjournals.onlinelibrary.wiley.com/doi/abs/10.1002/2056-4538.70080>, doi:<https://doi.org/10.1002/2056-4538.70080>.
- Chen, R.J., Ding, T., Lu, M.Y., Williamson, D.F.K., Jaume, G., Song, A.H., Chen, B., Zhang, A., Shao, D., Shaban, M., Williams, M., Oldenburg, L., Weishaupt, L.L., Wang, J.J., Vaidya, A., Le, L.P., Gerber, G., Sahai, S., Williams, W., Mahmood, F., 2024. Towards a general-purpose foundation model for computational pathology. *Nature Medicine* 30, 850–862. URL: <https://doi.org/10.1038/s41591-024-02857-3>, doi:[10.1038/s41591-024-02857-3](https://doi.org/10.1038/s41591-024-02857-3).
- Du, Z., Zhang, P., Huang, X., Hu, Z., Yang, G., Xi, M., Liu, D., 2025. Deeply supervised two stage generative adversarial network for stain normalization. *Scientific Reports* 15. URL: <https://doi.org/10.1038/s41598-025-91587-8>, doi:[10.1038/s41598-025-91587-8](https://doi.org/10.1038/s41598-025-91587-8).
- Dunn, C., Brettle, D., Hodgson, C., Hughes, R., Treanor, D., 2025. An international study of stain variability in histopathology using qualitative and quantitative analysis. *Journal of Pathology Informatics* 17, 100423. URL: <https://www.sciencedirect.com/science/article/pii/S2153353925000057>, doi:<https://doi.org/10.1016/j.jpi.2025.100423>.
- Folmsbee, J., Johnson, S., Liu, X., Brandwein-Weber, M., Doyle, S., 2019. Fragile neural networks: the importance of image standardization for deep learning in digital pathology, in: *Medical Imaging 2019: Digital Pathology*, SPIE. p. 38. URL: <https://doi.org/10.1117/12.2512992>, doi:[10.1117/12.2512992](https://doi.org/10.1117/12.2512992).
- Foot, A., Asif, A., Rajpoot, N., Minhas, F., 2022. Reet: robustness evaluation and enhancement toolbox for computational pathology. *Bioinformatics* 38, 3312–3314. URL: <https://doi.org/10.1093/bioinformatics/btac315>, doi:[10.1093/bioinformatics/btac315](https://doi.org/10.1093/bioinformatics/btac315).
- Howard, F.M., Dolezal, J., Kochanny, S., Schulte, J., Chen, H., Heij, L., Huo, D., Nanda, R., Olopade, O.I., Kather, J.N., Cipriani, N., Grossman, R.L., Pearson, A.T., 2021. The impact of site-specific digital histology signatures on deep learning model accuracy and bias. *Nature Communications* 12. URL: <https://doi.org/10.1038/s41467-021-24698-1>, doi:[10.1038/s41467-021-24698-1](https://doi.org/10.1038/s41467-021-24698-1).
- Janowczyk, A., Basavanthally, A., Madabhushi, A., 2017. Stain normalization using sparse autoencoders (stanosa): Application to digital pathology. *Computerized Medical Imaging and Graphics* 57, 50–61. URL: <https://doi.org/10.1016/j.compmedimag.2016.05.003>, doi:[10.1016/j.compmedimag.2016.05.003](https://doi.org/10.1016/j.compmedimag.2016.05.003).
- de Jong, E.D., Marcus, E., Teuwen, J., 2025. Current pathology foundation models are unrobust to medical center differences. URL: <https://arxiv.org/abs/2501.18055>, arXiv:2501.18055.
- Kautto, E.A., Bonneville, R., Miya, J., Yu, L., Krook, M.A., Reeser, J.W., Roychowdhury, S., 2016. Performance evaluation for rapid detection of pan-cancer microsatellite instability with mantis. *Oncotarget* 8, 7452–7463. URL: <https://doi.org/10.18632/oncotarget.13918>, doi:[10.18632/oncotarget.13918](https://doi.org/10.18632/oncotarget.13918).
- Kömen, J., Marienwald, H., Dippel, J., Hense, J., 2024. Do histopathological foundation models eliminate batch effects? a comparative study, in: *Advancements In Medical Foundation Models: Explainability, Robustness, Security, and Beyond*. URL: <https://openreview.net/forum?id=Ty0Z1J0ZQ0>.
- Kömen, J., de Jong, E.D., Hense, J., Marienwald, H., Dippel, J., Naumann, P., Marcus, E., Ruff, L., Alber, M., Teuwen, J., Klauschen, F., Müller, K.R., 2025. Towards robust foundation models for digital pathology. URL: <https://arxiv.org/abs/2507.17845>, arXiv:2507.17845.
- Lafarge, M.W., Pluim, J.P.W., Eppenhof, K.A.J., Moeskops, P., Veta, M., 2017. Domain-adversarial neural networks to address the appearance variability of histopathology images, in: *Cardoso, M.J., Arbel, T., Carneiro, G., Syeda-Mahmood, T., Tavares, J.M.R., Moradi, M., Bradley, A., Greenspan, H., Papa, J.P., Madabhushi, A., Nascimento, J.C., Cardoso, J.S., Belagiannis, V., Lu, Z. (Eds.), Deep Learning in Medical Image Analysis and Multimodal Learning for Clinical Decision Support*, Springer International Publishing, Cham. pp. 83–91.
- Lin, S., Zhou, H., Watson, M., Govindan, R., Cote, R.J., Yang, C., 2025a. Impact of stain variation and color normalization for prognostic predictions in pathology. *Scientific Reports* 15. URL: <https://doi.org/10.1038/s41598-024-83267-w>, doi:[10.1038/s41598-024-83267-w](https://doi.org/10.1038/s41598-024-83267-w).
- Lin, W., Liu, S., Zhu, R., Lin, Y., Wang, B., Wang, L., 2025b. Beyond diagnostic performance: Revealing and quantifying ethical risks in pathology foundation models. URL: <https://arxiv.org/abs/2502.16889>, arXiv:2502.16889.
- Loshchilov, I., Hutter, F., 2019. Decoupled weight decay regularization, in: *International Conference on Learning Representations*. URL: <https://openreview.net/forum?id=Bkg6RiCqY7>.
- Lu, M.Y., Williamson, D.F.K., Chen, T.Y., Chen, R.J., Barbieri, M., Mahmood, F., 2021. Data-efficient and weakly supervised computational pathology on whole-slide images. *Nature Biomedical Engineering* 5, 555–570. URL: <https://doi.org/10.1038/s41551-020-00682-w>, doi:[10.1038/s41551-020-00682-w](https://doi.org/10.1038/s41551-020-00682-w).
- Macenko, M., Niethammer, M., Marron, J.S., Borland, D., Woosley, J.T., Author, U., Schmitt, C., Thomas, N.E., 2009. A method for normalizing histology slides for quantitative analysis, in: *2009 IEEE International Symposium on Biomedical Imaging: From Nano to Macro, IEEE*. pp. 1107–1110. URL: <https://doi.org/10.1109/isbi.2009.5193250>, doi:[10.1109/ISBI.2009.5193250](https://doi.org/10.1109/ISBI.2009.5193250).
- Marini, N., Otolara, S., Wodzinski, M., Tomassini, S., Dragoni, A.F., Marchand-Maillet, S., Morales, J.P.D., Duran-Lopez, L., Vatrano, S., Müller, H., Atzori, M., 2023. Data-driven color augmentation for H&E stained images in computational pathology. *Journal of Pathology Informatics* 14, 100183. URL: <https://doi.org/10.1016/j.jpi.2022.100183>, doi:[10.1016/j.jpi.2022.100183](https://doi.org/10.1016/j.jpi.2022.100183).
- Miranda Ruiz, F., Lahrmann, B., Bartels, L., Krauthoff, A., Keil, A., Härtel, S., Tao, A.S., Ströbel, P., Clarke, M.A., Wentzensen, N., Grabe, N., 2023. Cnn stability training improves robustness to scanner and ihc-based image variability for epithelium segmentation in cervical histology. *Frontiers in Medicine* Volume 10 - 2023. URL: <https://www.frontiersin.org/journals/medicine/articles/10.3389/fmed.2023.1173616>, doi:[10.3389/fmed.2023.1173616](https://doi.org/10.3389/fmed.2023.1173616).
- Myles, C., Um, I.H., Marshall, C., Harris-Birtill, D., Harrison, D.J., 2025. Surgen: 1020 H&E-stained whole-slide images with survival and genetic markers. *GigaScience* 14. URL: <https://doi.org/10.1093/gigascience/giaf086>, doi:[10.1093/gigascience/giaf086](https://doi.org/10.1093/gigascience/giaf086).
- Network, T.C.G.A., 2012. Comprehensive molecular characterization of human colon and rectal cancer. *Nature* 487, 330–337. URL: <https://doi.org/10.1038/nature11252>, doi:[10.1038/nature11252](https://doi.org/10.1038/nature11252).
- Niehues, J.M., Quirke, P., West, N.P., Grabsch, H.I., van Treeck, M., Schirris, Y., Veldhuizen, G.P., Hutchins, G.G., Richman, S.D., Foersch, S., Brinker, T.J., Fukuoka, J., Bychkov, A., Uegami, W., Truhn, D., Brenner, H., Brobeil, A., Hoffmeister, M., Kather, J.N., 2023. Generalizable biomarker prediction from cancer pathology slides with self-supervised deep learning: A retrospective multi-centric study. *Cell Reports Medicine* 4, 100980. URL: <https://doi.org/10.1016/j.xcrm.2023.100980>, doi:[10.1016/j.xcrm.2023.100980](https://doi.org/10.1016/j.xcrm.2023.100980).
- Nishar, H., Chavanke, N., Singhal, N., 2020. Histopathological stain transfer using style transfer network with adversarial loss, in: *Martel, A.L., Abolmaesumi, P., Stoyanov, D., Mateus, D., Zuluaga, M.A., Zhou, S.K., Racoceanu, D., Joskowicz, L. (Eds.), Medical Image Computing and Computer Assisted Intervention – MICCAI 2020*, Springer International Publishing, Cham. pp. 330–340.
- Ochi, M., Komura, D., Onoyama, T., Shinbo, K., Endo, H., Odaka, H., Kakiuchi, M., Katoh, H., Ushiku, T., Ishikawa, S., 2024. Registered multi-device/staining histology image dataset for domain-agnostic machine learning models. *Scientific Data* 11. URL: <https://doi.org/10.1038/s41597-024-03122-5>, doi:[10.1038/s41597-024-03122-5](https://doi.org/10.1038/s41597-024-03122-5).
- Otolara, S., Atzori, M., Andrearczyk, V., Khan, A., Müller, H., 2019. Staining invariant features for improving generalization of deep convolutional neural networks in computational pathology. *Frontiers in Bioengineering and Biotechnology* Volume 7 - 2019. URL: <https://www.frontiersin.org/journals/biengineering-and-biotechnology/articles/10.3389/fbioe.2019.00198>, doi:[10.3389/fbioe.2019.00198](https://doi.org/10.3389/fbioe.2019.00198).

- Schömig-Markiefka, B., Prylukhin, A., Hulla, W., Bychkov, A., Fukuoka, J., Madabhushi, A., Achter, V., Nieroda, L., Büttner, R., Quaas, A., Tolkach, Y., 2021. Quality control stress test for deep learning-based diagnostic model in digital pathology. *Modern Pathology* 34, 2098–2108. URL: <https://doi.org/10.1038/s41379-021-00859-x>, doi:10.1038/s41379-021-00859-x.
- Shen, Y., Luo, Y., Shen, D., Ke, J., 2022. Randstainna: Learning stain-agnostic features from histology slides by bridging stain augmentation and normalization, in: Wang, L., Dou, Q., Fletcher, P.T., Speidel, S., Li, S. (Eds.), *Medical Image Computing and Computer Assisted Intervention – MICCAI 2022*, Springer Nature Switzerland, Cham. pp. 212–221.
- Sim, R.T.J., 2025. Stainnorm: A lightweight and robust network for stain colour normalization in histopathology, in: Guo, H., McLoughlin, I., Lakshmanan, U., Miao, X., Chekole, E.G., Meng, W., Wang, P.C., Lu, J., Wong, N.H.L. (Eds.), *Proceedings of the 10th IRC Conference on Science, Engineering and Technology*, Springer Nature Singapore, Singapore. pp. 323–330.
- Springenberg, M., Frommholz, A., Wenzel, M., Weicken, E., Ma, J., Strothoff, N., 2023. From modern cnns to vision transformers: Assessing the performance, robustness, and classification strategies of deep learning models in histopathology. *Medical Image Analysis* 87, 102809. URL: <https://doi.org/10.1016/j.media.2023.102809>, doi:10.1016/j.media.2023.102809.
- Stacke, K., Eilertsen, G., Unger, J., Lundstrom, C., 2021. Measuring domain shift for deep learning in histopathology. *IEEE Journal of Biomedical and Health Informatics* 25, 325–336. URL: <https://doi.org/10.1109/jbhi.2020.3032060>, doi:10.1109/jbhi.2020.3032060.
- Sun, Y., Zhu, C., Zhang, Y., Li, H., Chen, P., Yang, L., 2023. Assessing the robustness of deep learning-assisted pathological image analysis under practical variables of imaging system, in: *ICASSP 2023 - 2023 IEEE International Conference on Acoustics, Speech and Signal Processing (ICASSP)*, pp. 1–5. doi:10.1109/ICASSP49357.2023.10095887.
- Tellez, D., Litjens, G., Bándi, P., Bulten, W., Bokhorst, J.M., Ciompi, F., van der Laak, J., 2019. Quantifying the effects of data augmentation and stain color normalization in convolutional neural networks for computational pathology. *Medical Image Analysis* 58, 101544. URL: <https://www.sciencedirect.com/science/article/pii/S1361841519300799>, doi:<https://doi.org/10.1016/j.media.2019.101544>.
- Vu, Q.D., Jewsbury, R., Graham, S., Jahanifar, M., Raza, S.E.A., Minhas, F., Bhalerao, A., Rajpoot, N., 2022. Nuclear segmentation and classification: On color and compression generalization, in: Lian, C., Cao, X., Rekić, I., Xu, X., Cui, Z. (Eds.), *Machine Learning in Medical Imaging*, Springer Nature Switzerland, Cham. pp. 249–258.
- Wagner, S.J., Reisenbüchler, D., West, N.P., Niehues, J.M., Zhu, J., Foersch, S., Veldhuizen, G.P., Quirke, P., Grabsch, H.I., van den Brandt, P.A., Hutchins, G.G., Richman, S.D., Yuan, T., Langer, R., Jenniskens, J.C., Offermans, K., Mueller, W., Gray, R., Gruber, S.B., Greenson, J.K., Rennert, G., Bonner, J.D., Schmolze, D., Jonnagaddala, J., Hawkins, N.J., Ward, R.L., Morton, D., Seymour, M., Magill, L., Nowak, M., Hay, J., Koelzer, V.H., Church, D.N., Church, D., Domingo, E., Edwards, J., Glimelius, B., Gogenur, I., Harkin, A., Hay, J., Iveson, T., Jaeger, E., Kelly, C., Kerr, R., Maka, N., Morgan, H., Oien, K., Orange, C., Palles, C., Roxburgh, C., Sansom, O., Saunders, M., Tomlinson, I., Matek, C., Geppert, C., Peng, C., Zhi, C., Ouyang, X., James, J.A., Loughrey, M.B., Salto-Tellez, M., Brenner, H., Hoffmeister, M., Truhn, D., Schnabel, J.A., Boxberg, M., Peng, T., Kather, J.N., 2023. Transformer-based biomarker prediction from colorectal cancer histology: A large-scale multicentric study. *Cancer Cell* 41, 1650–1661.e4. URL: <https://doi.org/10.1016/j.ccell.2023.08.002>, doi:10.1016/j.ccell.2023.08.002.
- Wang, N.C., Kaplan, J., Lee, J., Hodgin, J., Udager, A., Rao, A., 2021. Stress testing pathology models with generated artifacts. *Journal of Pathology Informatics* 12, 54. URL: https://doi.org/10.4103/jpi.jpi_6_21, doi:10.4103/jpi.jpi_6_21.
- Wang, X., Du, Y., Yang, S., Zhang, J., Wang, M., Zhang, J., Yang, W., Huang, J., Han, X., 2023. Retccl: Clustering-guided contrastive learning for whole-slide image retrieval. *Medical Image Analysis* 83, 102645. URL: <https://doi.org/10.1016/j.media.2022.102645>, doi:10.1016/j.media.2022.102645.
- Wang, X., Yang, S., Zhang, J., Wang, M., Zhang, J., Yang, W., Huang, J., Han, X., 2022. Transformer-based unsupervised contrastive learning for histopathological image classification. *Medical Image Analysis* 81, 102559. URL: <https://doi.org/10.1016/j.media.2022.102559>, doi:10.1016/j.media.2022.102559.
- Wölflein, G., Ferber, D., Meneghetti, A.R., Nahhas, O.S.M.E., Truhn, D., Carrero, Z.I., Harrison, D.J., Arandjelović, O., Kather, J.N., 2025. A good feature extractor is all you need for weakly supervised pathology slide classification, in: Del Bue, A., Canton, C., Pont-Tuset, J., Tommasi, T. (Eds.), *Computer Vision – ECCV 2024 Workshops*, Springer Nature Switzerland, Cham. pp. 68–87.
- Xiong, C., Chen, H., Sung, J.J.Y., 2025. A survey of pathology foundation model: Progress and future directions, in: *Proceedings of the Thirty-Fourth International Joint Conference on Artificial Intelligence, International Joint Conferences on Artificial Intelligence Organization*. pp. 10751–10760. URL: <https://doi.org/10.24963/ijcai.2025/1193>, doi:10.24963/ijcai.2025/1193.
- Zimmermann, E., Vorontsov, E., Viret, J., Casson, A., Zelechowski, M., Shaikovski, G., Tenenholz, N., Hall, J., Klimstra, D., Yousfi, R., Fuchs, T., Fusi, N., Liu, S., Severson, K., 2024. Virchow2: Scaling self-supervised mixed magnification models in pathology. URL: <https://arxiv.org/abs/2408.00738>, arXiv:2408.00738.